49th AIAA Aerospace Sciences Meeting, Jan. 4–7, 2011, Orlando, Fl

Best Practices for Aero-Database CFD Simulations of Ares V Ascent

Cetin Kiris*, Jeffrey Housman†, Marshall Gusman†, Daniel Schauerhamer†
NASA Ames Research Center, Moffett Field, CA 94035

Karen Deere‡, Alaa Elmiligui§, Khaled Abdol-Hamid§, Ed Parlette¶
NASA Langley Research Center, Hampton, VA 23681

Mark Andrews‖, John Blevins**
NASA Marshall Space Flight Center, Huntsville, AL 35812

In support of NASA's next generation heavy lift launch vehicle (HLLV), a simulation protocol has been developed to generate databases of the aerodynamic force and moment coefficients for HLLV ascent. The simulation protocol has been established and validated with a series of computational analyses that ensure best practices are achieved. Results of the sensitivity analyses using a full-scale Ares V flight vehicle are next applied in a validation study with three scaled-down Ares V wind tunnel test articles. Three independent computational fluid dynamic (CFD) flow solvers were included in the study. These included OVERFLOW, a viscous Reynolds Averaged Navier-Stokes (RANS) solver for structured overset grids, USM3D, a viscous RANS solver for unstructured tetrahedral grids, and Cart3D, an inviscid Euler solver using unstructured Cartesian grids and adjoint-based adaptive mesh refinement. First, a series of tests was independently performed for each applicable CFD code, including a grid convergence study and sensitivity studies of turbulence models and convective flux discretization methods. Once the proper grid resolution, physical models, and numerical parameters were determined for each of the codes, the process was continued with a code-to-code comparison. Each CFD code was applied to the Ares V flight vehicle at several points in the ascent trajectory, with all three codes obtaining consistent force and moment predictions. Finally, an extensive validation of the CFD approach was performed, in which the three codes were used to generate aero-databases of force and moment coefficients for three distinct Ares V wind tunnel test articles. These computations were performed concurrent to the experimental databases generated in the 14-inch wind tunnel at Marshall Space Flight Center (MSFC). Comparisons of the CFD results with the experimental data are reported and the viscous flow results compare well.

*Branch Chief
†Aerospace Engineer, ELORET Corporation
‡Aerospace Engineer
§Research Aerospace Engineer
¶Aerospace Engineer, Vigyan
‖Aerospace Engineer, Jacobs Technology
**Lead Aerospace Engineer

Nomenclature

FV	: Flight Vehicle	
HLLV	: Heavy Lift Launch Vehicle	
SA	: Spalart Allmaras 1-eqn Turbulence Model	
SST	: Shear-Stress Transport 2-eqn Turbulence Model with Compressibility Correction	
SST-NC	: SST Turbulence Model with No Corrections	
SST-TC	: SST Turbulence Model with Temperature Correction	
M_∞	: Freestream Mach Number	
α	: Angle of Attack	(Body Axis)
β	: Side Slip Angle	(Body Axis)
α_T	: Total Angle of Attack	(Missile Axis)
ϕ_T	: Total Roll Angle	(Missile Axis)
CA	: Axial Force Coefficient	(Body Axis)
CY	: Side Force Coefficient	(Body Axis)
CN	: Normal Force Coefficient	(Body Axis)
CLL	: Roll Moment Coefficient	(Body Axis)
CLM	: Pitch Moment Coefficient	(Body Axis)
CLN	: Yaw Moment Coefficient	(Body Axis)
CAP	: Axial Force Coefficient	(Missile Axis)
CYP	: Side Force Coefficient	(Missile Axis)
CNP	: Normal Force Coefficient	(Missile Axis)
CLLP	: Roll Moment Coefficient	(Missile Axis)
CLMP	: Pitch Moment Coefficient	(Missile Axis)
CLNP	: Yaw Moment Coefficient	(Missile Axis)
Fx	: Force in X-Coordinate Direction	
Fy	: Force in Y-Coordinate Direction	
Fz	: Force in Z-Coordinate Direction	
r/r0	: Normalized Field Equation Residual	
tnu/tnu0	: Normalized Turbulence Model Residual	

I. Introduction

Computational fluid dynamics (CFD) modeling and simulation has become an integral part of NASA's ongoing development of next-generation launch vehicles. During the initial design stages of the Ares V, one concept for a heavy lift launch vehicle (HLLV), CFD analyses have been used to predict the aerodynamic loads of many vehicle design iterations. The computed loads along with several other predicted quantities that can not be easily obtained by experimental methods have been used to make critical design changes. For example, the surface pressure and line loads computed using CFD tools are utilized by structural engineers to estimate the structural loads on the vehicle. Computed force and moment coefficients for the flight vehicle are used by guidance, navigation, and control engineers to design an appropriate ascent trajectory. A key requirement for using CFD in aero-database generation is to establish best practices for accurate and efficient prediction of the force and moment coefficients on the vehicle. To meet the goals of this task, a multi-tiered protocol is outlined that establishes, verifies, and validates the CFD simulation procedure. The detailed descriptions and conclusions from the sensitivity and validation analyses are valuable for future CFD support of new HLLV concepts.

Code sensitivity and validation are important topics in CFD. With the increased use of CFD in the industrial setting where important decisions (possibly related to mission success) are being made, understanding the limitations and uncertainties of the results becomes a requirement. Many publications in the literature have been dedicated to defining and describing verification and validation procedures, a small subset includes the AGARD report on Validation of Computational Fluid Dynamics,[1] the AIAA Guideline,[2] and Verification

and Validation in Computational Science and Engineering.[3] For aero-database generation, the quantities of interest are the force and moment coefficients. Sensitivity studies are required to gain confidence in simulations, including studies on grid convergence, convective flux discretizations, and turbulence closure models. A grid convergence study consists of solving the governing flow equations on a sequence of coarse to fine grid resolutions. Since codes use different domain discretization techniques, such as structured curvilinear overlapping grids, unstructured tetrahedral grids, or unstructured Cartesian grids, the refinement procedure may also be different. Once the sequence of grids is defined and the CFD solution is obtained on each grid, the quantities of interest are plotted versus some measure of the grid resolution. For the CFD solution to be considered grid converged, the quantity of interest must converge to a single value as the resolution increases. Once grid convergence is achieved, a basic level of confidence is established by eliminating solution variation with respect to the discrete grid. CFD solutions are typically more sensitive to grid resolution than the turbulence model and convective flux discretization, so it is recommended to establish proper grid resolution first.

Turbulence modeling is a necessity for simulating high Reynolds number viscous flows, and there are many options for specifying the turbulence closure. Within the Reynolds (or Favre) Averaging approach there are 1st order closures (e.g. algebraic, one-equation, and two-equation models), as well as 2nd order closures (e.g. Reynolds-Stress Transport and Algebraic Reynolds-Stress models). In this work we focus on the Spalart-Allmaras one-equation model[4] and the SST two-equation model.[5] The sensitivity study consists of solving the CFD problem on the grid-converged mesh either using different turbulence models, changing the parameters within a single turbulence model, or some combination of both, and analyzing the change in the quantities of interest. Large variations in the quantities of interest would indicate strong sensitivity to the turbulence model, possibly requiring further grid refinement or an examination of the applicability of the models to the problem. Small variations indicate that the solution is well-behaved and the differences between turbulence models do not affect the predicted forces and moments, which is the desired result.

In a similar manner, the discretization of convective fluxes in the CFD solver should be analyzed to reduce solution sensitivity to this solver option. There are many options for convective flux discretization, including central differencing with explicit scalar or matrix artificial dissipation,[6,7] upwind flux-difference splitting schemes,[8] and upwind flux-vector splitting methods.[9,10] Each method has unique advantages and shortcomings, but they all converge to the same convective flux derivative with increasing grid resolution. At a fixed grid resolution, each of the convective flux discretization methods introduce artificial or numerical dissipation into the solution to maintain stability. The magnitude and location of the artificial dissipation is depends on both the scheme and the solution. A sensitivity analysis similar to the one performed for the turbulence model can be applied to the convective flux discretization schemes. Small variations are acceptable, but large variations indicate that higher mesh resolution is needed. In addition to the second-order central differencing scheme with scalar artificial dissipation, three upwind schemes were chosen for comparison in one of the viscous flow solvers: Advection Upstream Splitting Method (AUSM), Harten Lax and van Leer with contact restoration (HLLC), and Roe flux difference splitting. After establishing the individual CFD code requirements for self-consistent results, the next step in the procedure is a code-to-code comparison.

For Ares V database generation, comparisons are performed for the full-scale flight vehicle at several points in the ascent trajectory ranging from subsonic to supersonic flow regimes. Three independent well-documented and tested CFD codes were chosen: OVERFLOW,[11,12] USM3D,[13,14] and Cart3D.[15,16] OVERFLOW is a viscous Reynolds Averaged Navier-Stokes (RANS) solver for structured overset grids, USM3D is a viscous RANS solver for unstructured tetrahedral grids. Cart3D is an inviscid solver using unstructured Cartesian grids and adjoint-based adaptive mesh refinement. Both OVERFLOW and USM3D are accurate and efficient for high Reynolds number aerodynamic flows. Cart3D is efficient and highly automated for database generation, but lacks the viscous modeling capabilities of the other two codes. The acceptable tolerance level for sensitivity analyses and validation procedures were given to the CFD team as 10-15%. Good comparisons between the different CFD codes reduce the uncertainty in the numerical results.

Sensitivity analyses are only the first step to ensuring accurate numerical aero-databases; validation is the second step. Validation of CFD results requires a demonstration that the computational analyses represent the actual physical phenomenon. Since Ares V is in the design stage, it is not feasible to construct full-scale flight vehicles and collect flight data for comparison. Instead, an 0.3364% scale Ares V wind tunnel test article was created and an experimental database was generated in the 14-inch TriSonic Wind Tunnel (TWT) at Marshall Space Flight Center (MSFC). The CFD results were computed prior to the experimental

measurements being taken to ensure no bias towards the CFD or experimental results, and all configurations considered in the experimental test matrix were included in the CFD database to fully explore the validation study. A strong comparison between experiment and CFD results would validate the current best practices for HLLV clean configurations (no geometric protuberances and no plumes), and provide confidence that the current CFD approach can generate physically correct results for the full scale Ares V flight vehicle.

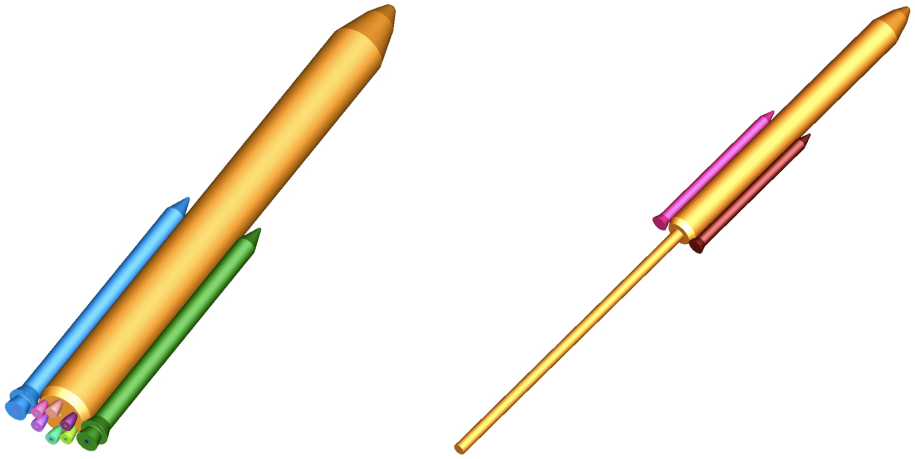

(a) (b)

Figure 1. Computational geometries for simplified Ares V Vehicle-I: (a) full-scale flight vehicle, and (b) wind tunnel test article.

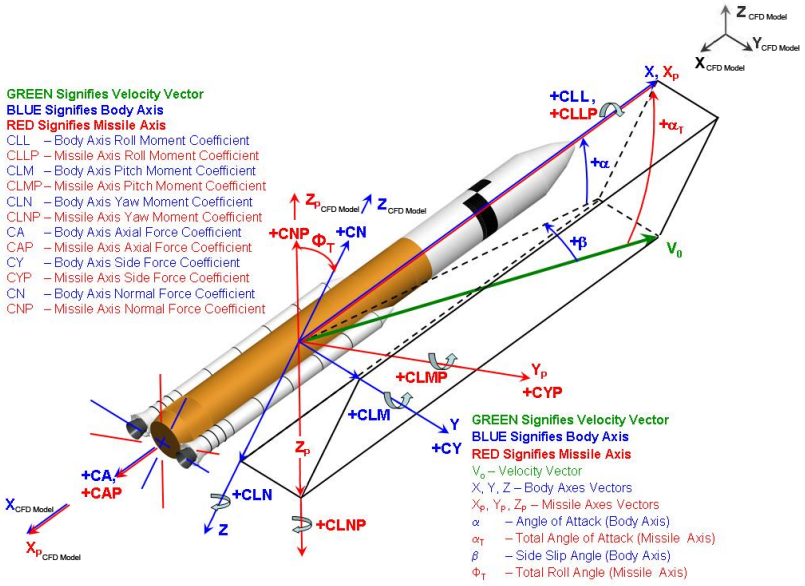

Figure 2. Various axis systems for reporting force and moment coefficients including: CFD model, missile, and body axis systems.

The results of these best practices build upon the knowledge and experience gained through the previous sensitivity and validation studies performed on other launch vehicles. These include work on the Space Shuttle;[17] overset grid generation;[18] Orion;[19] ascent aerodynamics of Ares I;[20] and simulation guidelines for meshing the launch abort vehicle using Cart3D.[21] Note that the sensitivity of certain information has required figures to be published with normalized scales, or none at all.

II. Computational Models

The computational geometries for the initial design cycles of the Ares V are configurations without geometric protuberances that consist of a core section and two Solid Rocket Boosters (SRBs). Protuberances such as fuel/oxidizer feed lines, struts, structural stiffeners, and flanges have not been included. Variations on the nose shape, engine fairings, number of engines, and size of the core and SRBs have changed throughout the design cycles. Code-to-code comparisons have been performed on the full-scale Ares V Vehicle-I, which includes six RS-68 engine nozzles positioned in a circle and two 5.5-segment SRBs, as shown in Figure 1 (a). The corresponding wind tunnel test article is also used for further code-to-code comparisons as well as validation studies with experimental data. This model includes a cylindrical sting protruding one body-length from the base of the core, and excludes the nozzle section of the RS-68s and SRBs. The 14-inch scaled wind tunnel test article of Vehicle-I is shown in Figure 1 (b), and the model axis system is shown in Figure 2. Test conditions are used that coincide with an experimental test in the TWT. The force and moment coefficients are computed in both missile and body axis coordinate systems for comparison with experimental data and previously computed flight vehicle CFD results.

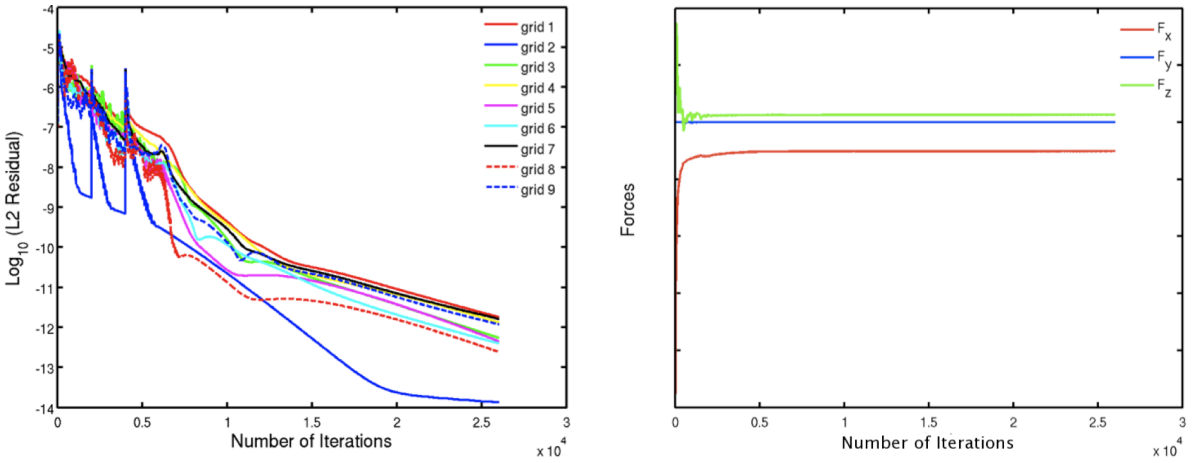

(a) (b)

Figure 3. Representative plot of the convergence history of the residual (a) and forces (b) for Ares V flight vehicle using OVERFLOW.

III. Flow Solvers

A. OVERFLOW

The NASA flow solver, OVERFLOW-2, is used to simulate the viscous flow-field around the Ares V vehicle. OVERFLOW is an implicit structured-overset RANS solver. The results reported in this work were computed with second-order central differencing, explicit scalar artificial dissipation using the default dissipation coefficients,[12] and the Spalart-Allmaras one-equation turbulence model, unless indicated otherwise. A diagonalized implicit solver is used and the code is run in parallel using domain decomposition with the Message Passing Interface (MPI) standard for parallel communication. The reported results were run on either the Columbia or Pleiades supercomputers at NASA Ames Research Center, using 64 to 96 processors and approximately 8 to 14 hours of runtime for each steady-state run. Structured viscous overset grid systems were custom built to model the flight vehicle and wind tunnel test articles. A grid generation script using the Chimera Grid Tools (CGT) script library[22] were developed to create the overlapping grid system. Typical convergence results are shown in Figure 3 with plots of residual convergence (a) and force convergence (b). The large spikes in the early stages of the residual plot are caused by a successive reduction of the artificial dissipation parameters from relatively large values to the default values described in the OVERFLOW manual. The purpose of modifying the dissipation parameters is to allow a large CFL number to be used throughout the computations, which leads to faster overall turn-around time.

Pressure contours on the surface and a slice through the domain, shown in Figure 4, reveal the flow features at subsonic, transonic, and supersonic trajectory points. At Mach 0.9, the fish-tail shock structures just aft of the main shroud and SRB nose cones identify regions of supersonic flow. At supersonic conditions, bow shocks are generated from the main shroud and SRB nose cones, and oblique shocks can be detected coming from the rear fairings and SRB skirts. Low pressure is observed in the base region in all four Mach regimes.

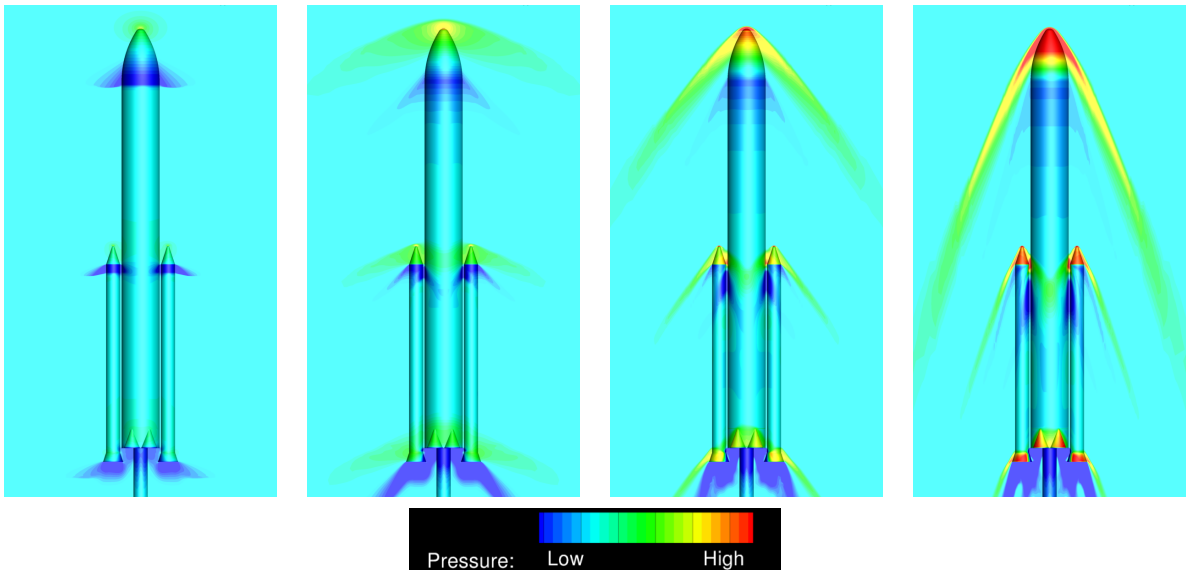

Figure 4. Pressure contours on the surface and a slice through the domain, at freestream Mach numbers 0.9, 1.2, 1.96, and 3.48 with zero angle of attack.

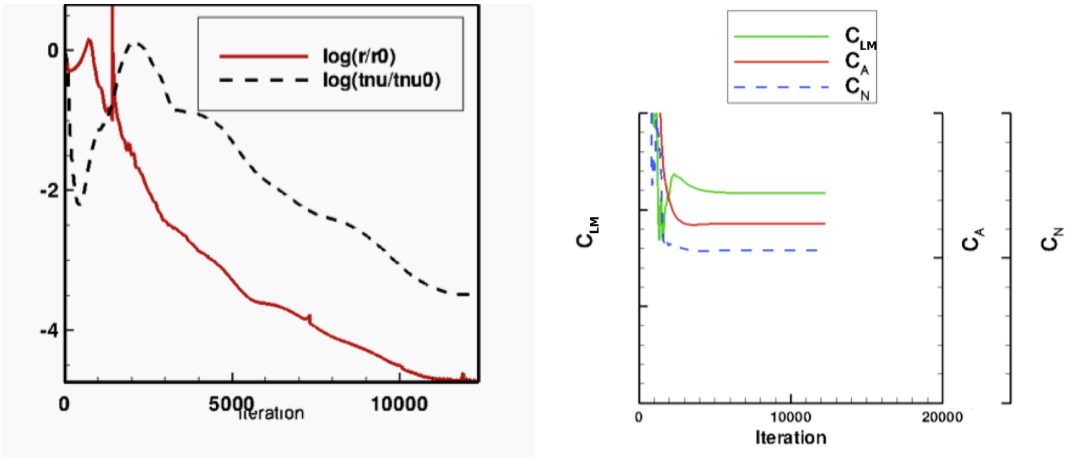

(a) (b)

Figure 5. Convergence history of the residual (a), and forces (b) for Ares V simulation using USM3D.

B. USM3D

Another NASA code, USM3D, is used as an additional data source for viscous flow solutions. USM3D is an unstructured tetrahedral viscous RANS flow solver with several options for upwind spatial discretization of the convective fluxes, various turbulence models, and limiters. USM3D is parallelized for several types of computational platforms using a domain decomposition approach. For the current results, the Harten

Lax and van Leer with the contact restoration (HLLC) spatial-differencing scheme was used for inviscid flux discretization for Mach numbers greater than 2.5, and Roe's flux-difference splitting scheme was used for Mach numbers under 2.5. Additionally, the Spalart-Allmaras turbulence model was used to close the RANS model. Each steady state run was performed using 128 processors for approximately 8 to 12 hours of runtime on the Columbia supercomputer. Typical convergence results are shown in Figure 5, with plots of residual convergence (a) and force convergence (b).

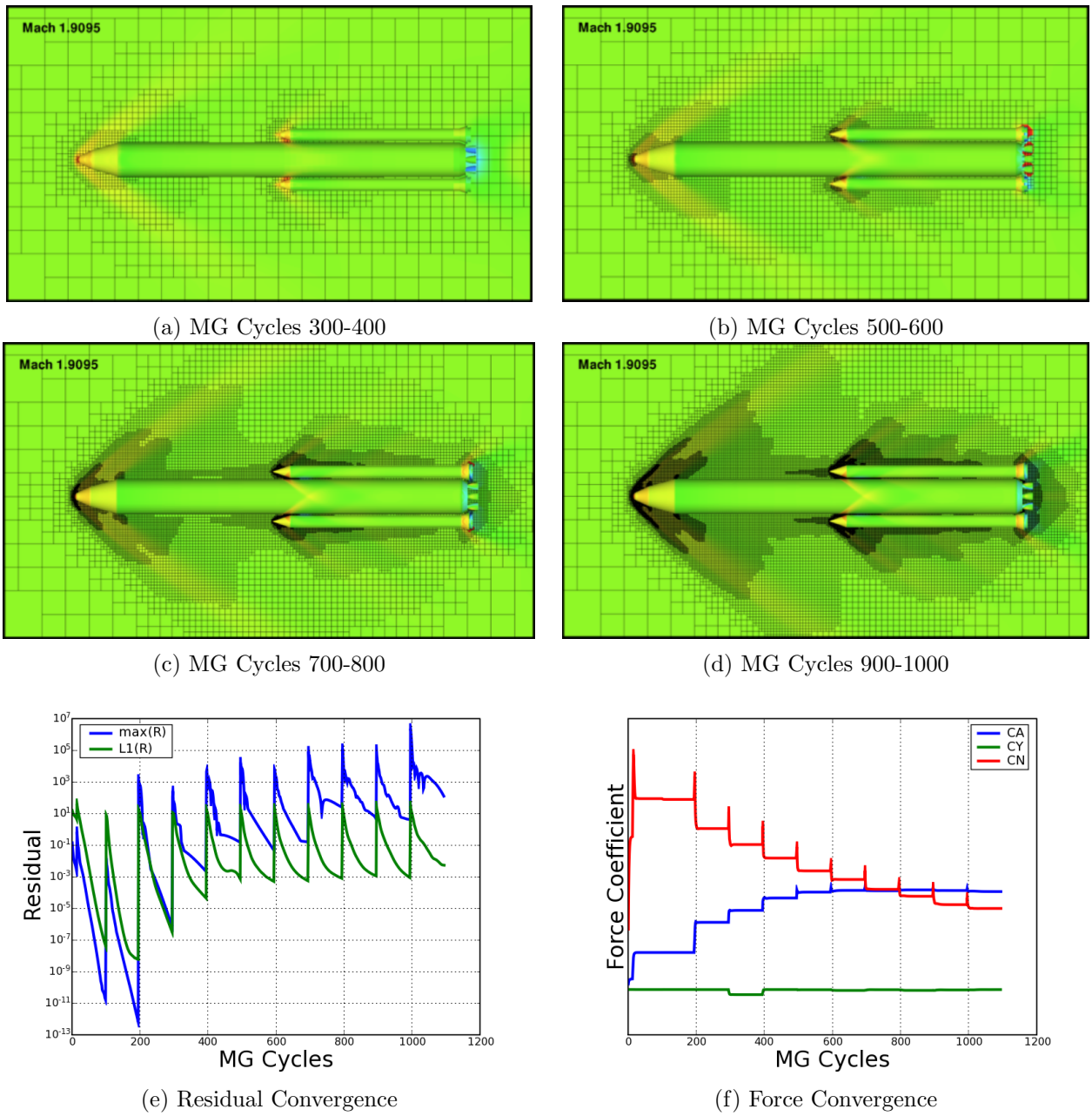

(a) MG Cycles 300-400

(b) MG Cycles 500-600

(c) MG Cycles 700-800

(d) MG Cycles 900-1000

(e) Residual Convergence

(f) Force Convergence

Figure 6. Typical sequence of adapted grids (a-d) and convergence history (e) & (f) for Ares V using Cart3D.

C. Cart3D

The inviscid CFD code Cart3D, the final NASA flow solver, can be used to quickly and efficiently populate an entire aerodynamic database of flow solutions. This code enables very efficient preliminary solutions to be obtained and utilizes a shared memory, OpenMP-based parallel approach. The accuracy of these solutions

is dependent on the validity of the inviscid assumption, but they provide guidance for the more costly viscous codes. Cart3D is an inviscid Cartesian grid flow solver with an automated adjoint-based adaptive mesh capability. It is fast, robust, and efficient, making it useful for database generation where hundreds of flow solutions are required. The adjoint-based adaptive meshing algorithm helps to improve computational efficiency by only refining regions of the flow domain that will reduce discretization error for a user-specified functional of interest (i.e. a linear combination of force and moment coefficients). After solving the flow equations on a coarse mesh (typically a few thousand cells), Cart3D next solves a system of adjoint equations based on the functional, and a local estimate of error contribution to the given functional is calculated for each cell. Regions of unacceptable error contribution are refined, and the procedure is repeated until the cumulative error drops below the given tolerance level. In this way, each point in the database is solved on an optimum mesh where shocks, geometry, and other critical regions are well defined. The sequence of grids and solutions generated during the refinement procedure provide a detailed grid convergence study. For the results reported here, each of the steady-state runs utilized van Leer flux-vector splitting discretization and were performed on 16 to 32 processors over approximately 2 hours of runtime on Columbia. Typical cell counts for the converged solutions were in the 3-5 million range. Examples of the grid adaptation process and residual convergence results are plotted in Figure 6. The residual convergence exhibits a sawtooth profile due to the sequentially adapted grids; the solution converges on each mesh level for 100 multigrid W-cycles before being reset to a normalized value on the next finer mesh level.

IV. Independent Flow Solver Sensitivity Analysis

The sensitivity studies described in the introduction are applied to each code separately to determine the correct grid and solver parameters for modeling Ares V during ascent. Tests are performed on both the full-scale flight vehicle and the wind tunnel test article. Grid convergence studies are conducted for OVERFLOW and USM3D to determine the grid resolution requirements. Cart3D's solution procedure implicitly performs this study in each simulation (see Figure 6). Next, turbulence model dependence for OVERFLOW and USM3D are analyzed using sensitivity analysis. A final sensitivity study is performed on the convective flux discretizations available in OVERFLOW.

A. Grid Convergence - OVERFLOW

A series of increasingly refined grid systems was generated to determine the proper spatial resolution for OVERFLOW simulations. A solution is considered grid-independent when the force and moment coefficients differ by less than or equal to 1% compared to the solution on the finest grid. Grid systems are composed of two types of structured overset grids; near-body and off-body. Near-body grids are curvilinear body-conforming grids. Off-body grids are used to discretize the remaining domain between near-body grids and far-field boundaries. Two approaches exist within the off-body grid type. One method of off-body grid generation uses a single zone with uniform refinement at the near-body/off-body grid interface and stretching to extend to the far-field. An alternative to the single-zone approach uses multiple overlapping Cartesian grids of different resolutions to fill the domain. This approach is referred to as the 'bricks' approach. It allows a fine grid resolution to interface with the near-body grids, and coarsens by factors of two away from the body to achieve fewer overall grid points. Both methods are examined in the following grid-convergence study.

To represent the wide range of flow conditions encountered in database generation, four representative cases are simulated with each grid resolution. Three cases are oriented for $\alpha_T = \phi_T = 0^\circ$ and are simulated at Mach numbers 0.9, 1.68, and 3.48. The fourth case is oriented to generate significant forces and moments in each direction (axial, side, and normal), at $\alpha_T = 6^\circ$, $\phi_T = 45^\circ$, and is simulated at Mach 1.68. The grids for the first three test cases contain 2 million, 6 million, 9 million, 18 million, 36 million, and 54 million grid points, all using a single-zone Cartesian background grid. One additional grid is generated which uses the near-body resolution of the 36 million grid point case, but with the multi-zone bricks approach which yields a total of 27 million grid points. These grid systems are shown in Figure 7. For the fourth test case, the grids contain 2.5 million, 6 million, 10 million, 20 million, 43 million, and 50 million points for the single-zone off-body grid, and 30 million for the multi-zone off-body grid. Differences in the number of grid points between the two configurations were due to the off-body grids.

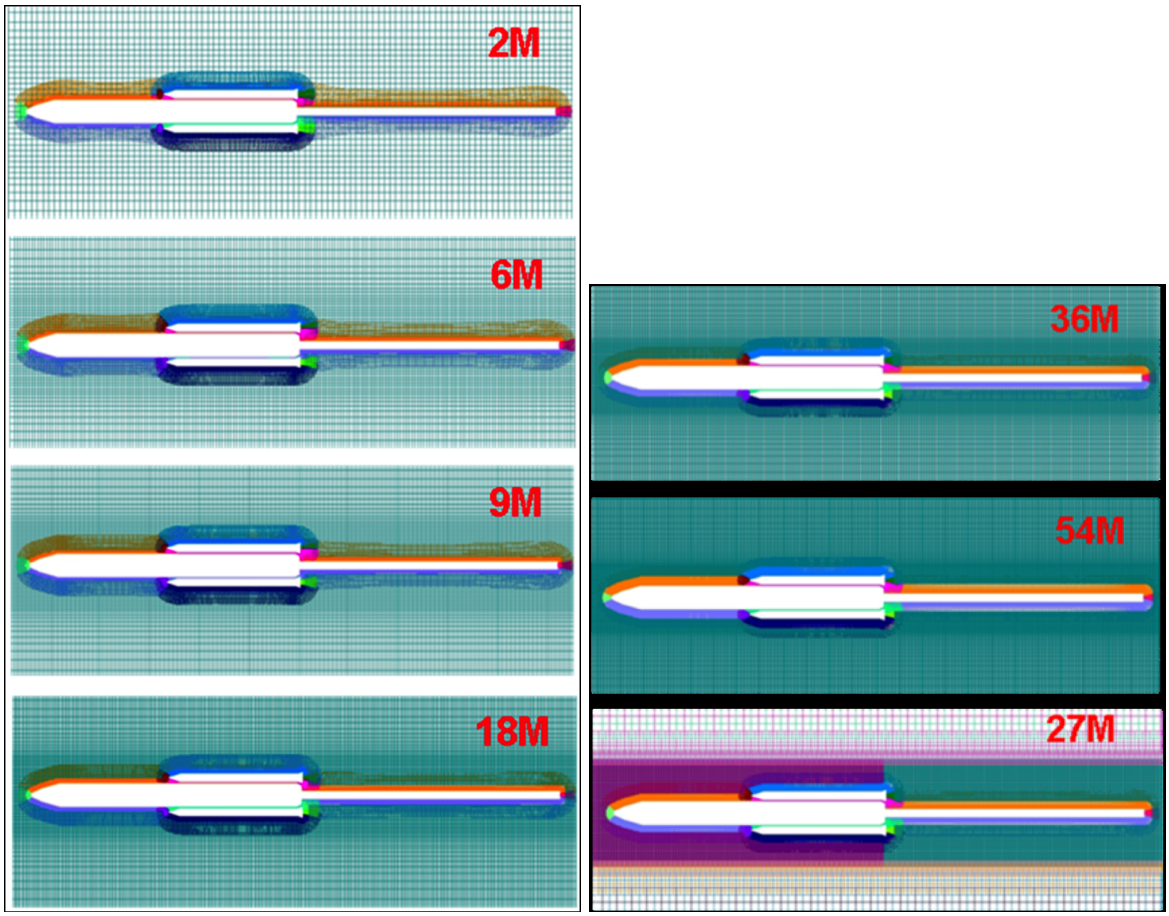

(a) (b)

Figure 7. Magnified view of the sequence of grids used in the grid convergence study, including an additional case (27M) with automatically generated off-body grids.

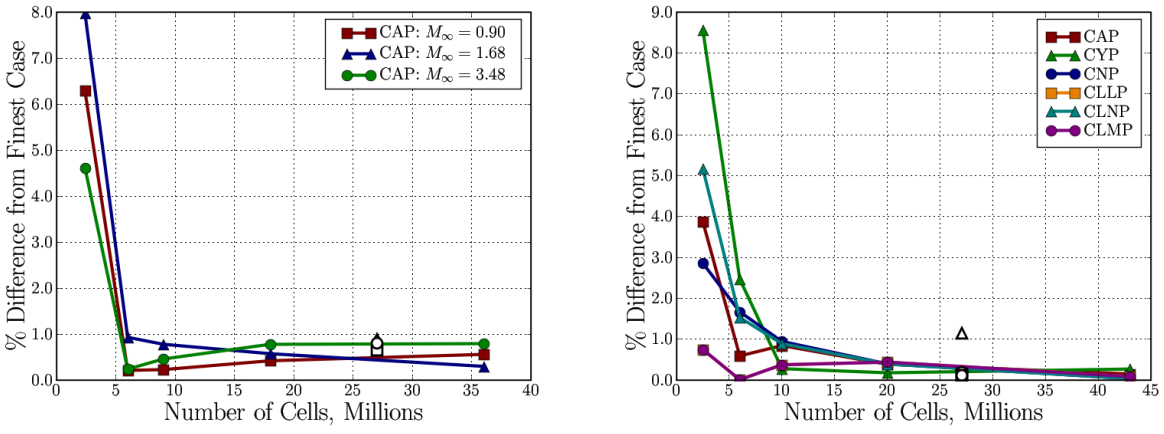

(a) (b)

Figure 8. Convergence of OVERFLOW solutions as percent difference of force and moment coefficients from the finest grid system, (a) three Mach numbers at $\alpha_T = 0°$, $\phi_T = 0°$, (b) Mach 1.68 at $\alpha_T = 6°$ $\phi_T = 45°$. Note: Black and white markers (CA-Square, CY-Triangle, CN-Circle) indicate 27M cell bricks off-body.

Force and moment coefficients are obtained from converged OVERFLOW solutions on each grid. To determine whether a grid-independent solution has been achieved, percentage differences are computed with respect to the most refined 54 million grid point solution. A plot of the differences in axial force (all other force and moment components are zero when $\alpha_T = \phi_T = 0°$) is shown in Figure 8(a). This figure shows that the percent difference is below one percent for grids with greater than or equal to 9 million grid points, and thus, all grids greater than or equal to 9 million grid points are grid-converged for the $\alpha_T = 0°$ case. The percent difference in axial force for the automatically generated off-body grid case, denoted by the black and white markers in the plot, is also below one percent. Figure 8(b) shows the percent difference for the non-zero force and moment coefficients for the $\alpha_T = 6°$, $\phi_T = 45°$ case. The plot shows less than 1% difference for all coefficients on grids with greater than or equal to 10 million points. Improvements are seen with the 20 million point grid, and the bricks off-body grid is also below the tolerance for all coefficients but one, which is slightly above 1%. The results of this study determined that the multi-zone off-body approach provided the best balance of adequate refinement, low computational cost, and ease of use, and was therefore chosen for generating the OVERFLOW aero-database for the wind tunnel test article.

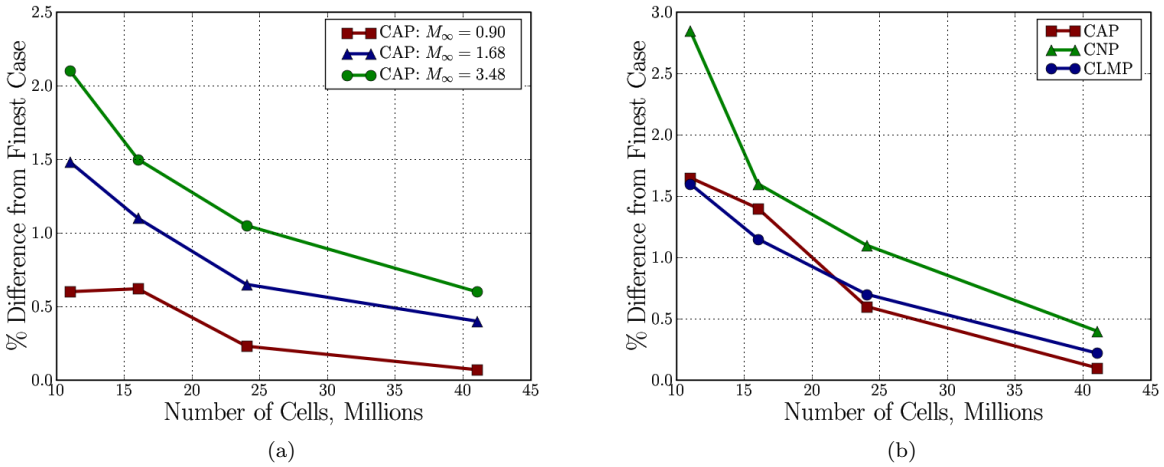

Figure 9. Convergence of USM3D solutions as percent difference of force and moment coefficients from the finest grid system, (a) three Mach numbers at $\alpha_T = 0°$, $\phi_T = 0°$, (b) Mach 1.68 at $\alpha_T = 6°$ $\phi_T = 0°$.

B. Grid Convergence - USM3D

A similar grid-convergence study is performed for USM3D, using a sequence of five different grid densities evaluated at multiple flow conditions. The grid sequence consists of grids with 11 million, 16 million, 24 million, 41 million, and 55 million cells. Viscous solutions are computed at Mach 0.9, 1.68 and 3.48 with zero degrees roll angle (ϕ_T) and pitch angles (α_T) of zero and six degrees.

Force and moment coefficients were calculated for each converged solution on each grid. In order to determine whether a grid-independent solution had been obtained, the percent differences in force and moment coefficients were computed between the finest mesh (55 million cells) solution and the other mesh density solutions. A plot of the percent differences in axial force is shown in Figure 9(a). This figure shows that the mesh with 55 million cells was sufficiently refined because decreasing the cell count to 41 million cells had less than a 0.3% difference in axial force between the two solutions. Computational resources required for each mesh density at the flow conditions Mach = 0.68, $\alpha_T = 6°$ and $\phi_T = 0°$ vary considerably. The 55 million-cell mesh solution requires substantially more resources, without a comparative gain in solution accuracy. The mesh with 24 million cells offers a 78% decrease in CPU hours for a converged solution that predicts axial force within 0.6% of the solution on the 55 million-cell mesh.

The mesh with 24 million cells is representative of the meshes that follow the best practices methods for obtaining accurate solutions with USM3D. Surface cell sizes are much smaller than the geometry features to accurately capture the curvature of the surfaces, while y^+ is defined to be less than 1 for accurate boundary layer definition. The axial force predictions for the 24 million-cell mesh, at all Mach numbers and angles of

attack, are within 1% of the predictions on the mesh with 55 million cells. All of the axial force predictions on the various mesh densities at several Mach numbers were within 2.1% of the solutions on the finest mesh. The grid density impacts on normal force and pitching moment coefficients can best be evaluated for the Mach= 1.68 case with $\alpha_T = 6°$ and $\phi_T = 0°$. As shown in Figure 9(b), normal force and pitching moment coefficients predicted with the 24 million cell mesh are within 1% of the coefficients predicted with the 55 million cell mesh.

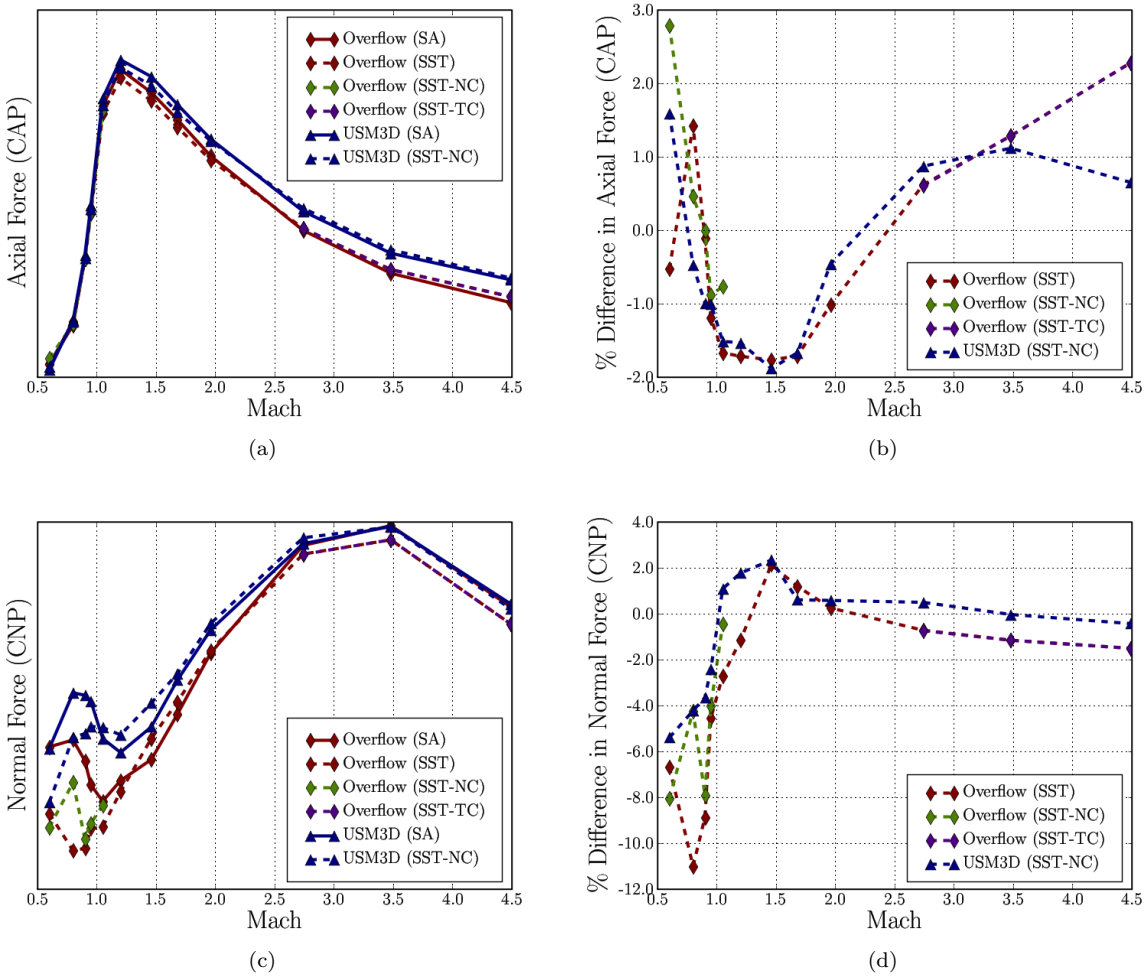

Figure 10. Comparison of SA and SST turbulence models using two codes, showing axial and normal force versus Mach number for $\alpha_T = 6°$, $\phi_T = 0°$ orientation. Scale-less coefficients (left), and percent-difference (right) from each code's respective SA solution.

C. Turbulence Modeling - OVERFLOW and USM3D

In order to examine the effects of turbulence modeling, both OVERFLOW and USM3D were run with the shear stress transport (SST) turbulence model in place of the Spalart-Allmaras (SA) turbulence model, which was used in the grid convergence study. For this sensitivity study, the $\alpha_T = 6°$ with $\phi_T = 0°$ configuration was chosen and the steady solutions for the entire Mach number range were computed using both of the viscous flow solvers with the SST model including a compressibility correction, but no temperature correction. The subsonic portion of the trajectory was also run with the compressibility correction turned off (NC), and the supersonic portion with temperature correction turned on (TC) using OVERFLOW. In Figure 10(a) the axial force is plotted as a function of Mach number for both OVERFLOW and USM3D computations using the SA and SST turbulence models. In Figure 10(b) the percent difference between the SST model and the

SA model is independently plotted. This shows that the largest variations are within 3%, which implies that the axial force is not sensitive to the turbulence model for this configuration. No significant change resulted from turning off the compressibility correction in the subsonic regime or from turning on the temperature correction in the supersonic regime. The normal force coefficient in Figures 10 (c) and (d), show larger variations, up to 11% in the subsonic regime. This is likely due to the sensitivity of the normal force at low speeds where the coefficient is smaller than in the supersonic regime. Overall, sensitivity to the turbulence model is consistent between both codes, and is below the acceptable limit at this stage in the design cycle. Thus, the more computationally efficient Spalart-Allmaras model is used for database generation in both OVERFLOW and USM3D. For simulations including rocket engine plume effects, it may be possible to see some variations between turbulence models, see Gusman et al.[23] and Deere et al.[24]

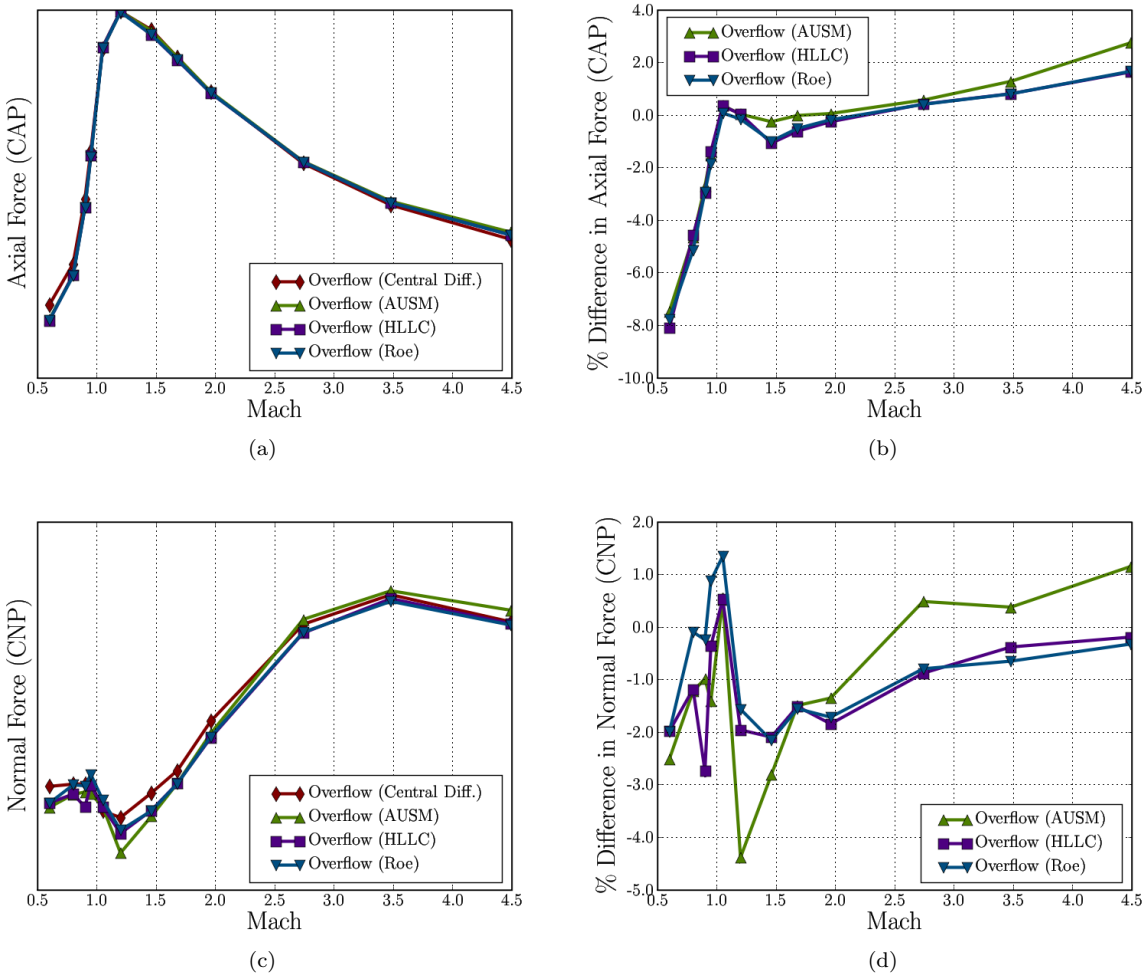

Figure 11. Comparison of convective flux discretizations, showing axial and normal force versus Mach number for $\alpha_T = 6°$, $\phi_T = 45°$ orientation. Scale-less coefficients (left), and percent-difference (right) from the central difference solution.

D. Convective Flux Discretization - OVERFLOW

The sensitivity of the predicted force coefficients with respect to the convective flux discretization are examined in this section. Typically, OVERFLOW uses central differencing of the convective fluxes with explicit artificial dissipation to minimize spurious oscillations at shocks. Upwind based flux discretizations are also available including the Advection Upstream Splitting Method (AUSM), Harten Lax and van Leer with contact restoration (HLLC), and Roe flux difference splitting. These methods all use the characteristic

information of the flux in order to bias the differencing stencil in the proper direction. The artificial dissipation associated with the upwind methods is implicit, and a strong connection exists between the upwind methods and central differencing with artificial dissipation. In fact, many upwind schemes can be rewritten as central differencing with a particular form of artificial dissipation. In order to examine the sensitivity of results to the convective flux discretization, the $\alpha_T = 6°$ and $\phi_T = 45°$ case is solved using the three upwind convective flux options in OVERFLOW, and compared to the central differencing results. In Figure 11 (a) the axial force coefficient is plotted as a function of the Mach number for each spatial discretization scheme. The corresponding percent difference of each upwind scheme from the central difference results is plotted in Figure 11 (b). These plots indicate that the percent difference is between $3 - 8\%$ over the entire Mach number range, with the largest differences in the low subsonic regime. There is almost no difference between the Roe and HLLC results. The 8% difference in the low subsonic point of the ascent trajectory is still within the acceptable margin of error, and further study is required to get a full understanding of the cause for this difference. Figures 11 (c) and (d) plot the normal force coefficient and percent difference of the upwind schemes from the central differencing result, respectively. In this case the variations are between 1.5% and 4.5% over the entire Mach number range. More sensitivity between the upwind schemes is observed for the normal force coefficient, but all variations are within acceptable margins.

The independent code sensitivity studies have demonstrated that each code achieves a grid independent solution and the two viscous codes appear to be insensitive to the choice of turbulence model closure (assuming a RANS model). Additionally, it was observed that OVERFLOW predictions are also insensitive to the choice of convective flux discretization. The results of the turbulence and convective flux sensitivity analyses provides further evidence that the proper grid resolution was found for each of the CFD codes.

V. Code-to-Code Comparisons

The final step in our procedure is a code-to-code comparison. An aero-database for the full-scale Ares V flight vehicle was chosen along with twelve points from the ascent trajectory representing the flight envelope. This included conditions from just after launch up to SRB separation, and encompasses Mach numbers ranging from 0.6 to 4.0 and Reynolds numbers from 3.16×10^4 to 2.75×10^5. No flight data exists since the vehicle is still in the design stage, so a code-to-code comparison is one option to verify the CFD results. Each case was run to steady-state using the three CFD codes, and force and moment coefficients were computed on the forebody of each vehicle. The base and nozzle regions for the flight vehicle and the base and sting for the wind tunnel model are excluded from the force and moment integration. Figure 12 (a) shows the rear extent of the integration surface for the force and moment computations, which begins at the nose of the core and SRB sections and is colored purple in the figure.

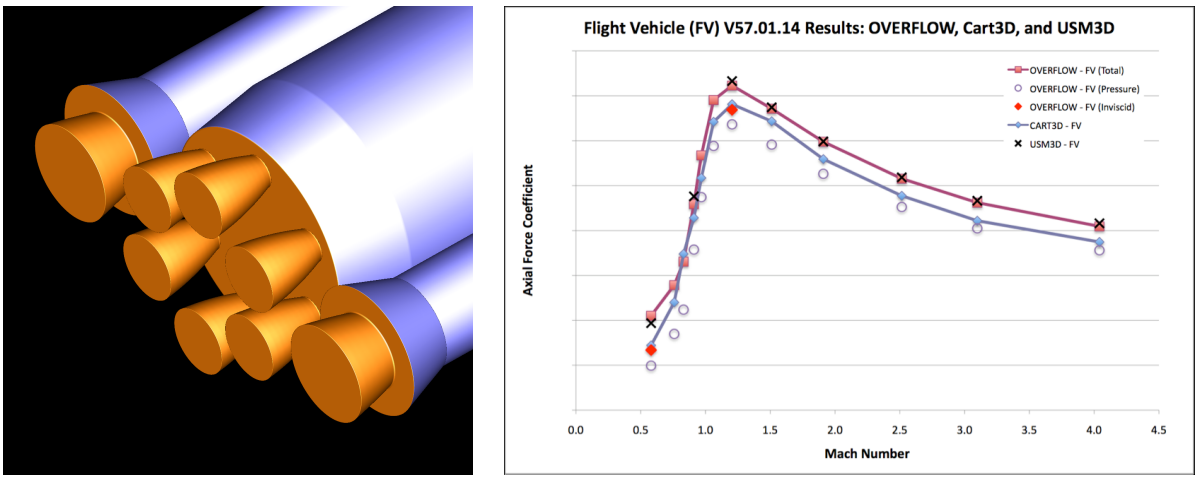

(a) Integration Surface

(b) Axial Force Coefficient

Figure 12. (a) Extent of the force and moment integration surface, in purple. (b) Code-to-code comparison showing axial force coefficient versus Mach number flight vehicle.

The axial force coefficient is plotted versus Mach number for OVERFLOW, USM3D and Cart3D in Figures 12 (b). OVERFLOW and USM3D exhibit axial force predictions within 2% of each other, while the inviscid Cart3D results are within 10% of the viscous solutions, excluding the low Mach number regime. The inviscid results are speculative in the low speed regime where high Reynolds number flow separation may have a large influence on the computed forces and moments. Two additional inviscid OVERFLOW simulations were performed to verify the Cart3D results. These results are shown as red diamonds in Figure 12 (b). The two inviscid solutions agree very well, implying that the differences between the Cart3D solutions and those produced by the two viscous codes can be attributed to the inviscid flow assumption. Also note that the pressure contribution to the viscous OVERFLOW axial force is less than the inviscid axial force. This indicates that the viscous boundary layer is dissipating large pressure variations along the body surface, and reducing jumps in pressure across shocks in the transonic and supersonic regimes. The code-to-code comparison provides confidence levels in the CFD results when no experimental data is available. The good comparison between CFD codes proves the utility of the independent sensitivity studies. A similar procedure should be performed when increasing the model fidelity with protuberances or exhaust plumes.

VI. CFD Validation with Experimental Data

Although the sensitivity studies and code-to-code comparisons provide confidence, they do not quantify the error between CFD results and physical results. In order to gain a more quantitative accuracy assessment, a validation study must be performed. Note that all three codes are used throughout the validation procedure, so code-to-code comparisons can also be assessed. In the validation study, three different wind tunnel test articles at 0.336% scale, denoted Vehicle-I, Vehicle-II, and Vehicle-III, are simulated with each code and compared against experimental results attained at the 14-inch TWT. Only a subset of the results from the experimental and numerical wind tunnel are presented here, but the trends are similar over the entire trajectory. It is important to note that the CFD results were computed either prior to or concurrent with the experiments, and no data was exchanged between the experimental teams or the CFD teams until the database was complete. This ensured that no bias towards the experiment or a particular CFD code is introduced.

An overview of the experimental facility and particular setup for the wind tunnel test article is described. The database run for Vehicle-I consists of eight pitch angles, five roll angles, and twelve Mach numbers for a total of 480 cases.

- Pitch angle $\alpha_T = -4$, -2, 0, 2, 4, 6, 8, and 10 degrees
- Roll angle $\phi_T = 0$, 22.5, 45, 67.5, and 90 degrees
- Mach number $M_\infty = 0.6$, 0.8, 0.9, 0.95, 1.05, 1.20, 1.46, 1.68, 1.96, 2.74, 3.48, and 4.49

For Vehicle-II and III, aerodynamic databases were generated for the full-scale flight vehicles across the trajectory of 12 Mach numbers with α and β variations from 0 to 10° at every 2°. For each Mach number, this corresponds to 36 unique simulations and a total of 432. Simulations were then repeated for wind tunnel test articles before the experiment was conducted. Mach numbers corresponded to those in Vehicle-I, with α ranging from 0 to 10° at every 2° and $\beta = 0°$. Comparisons are made between the CFD results for the wind tunnel test article and the experimental data. Due to the large number of cases only a subset of the results are presented.

A. Experimental Facility and Setup

Experimental data was obtained from the TriSonic Wind Tunnel, see Figure 13. This is an intermittent blow-down tunnel that operates by high-pressure air flowing from storage tanks to atmospheric or vacuum conditions.[25,26] The transonic test section provides a Mach number range from 0.2 to 2.5, with Mach numbers between 0.2 and 1.3 obtained by using a variable diffuser. The transonic range from 0.95 to 1.3 is achieved through the use of plenum suction and perforated walls. Each Mach number above 1.3 requires a specific set of contoured nozzle blocks. A solid wall supersonic test section provides the entire range from 2.74 to 5.0, with one set of automatically actuated contour nozzle blocks. The model was instrumented with an internal strain gage balance designed to provide six-component force and moment data for all runs. A total of six model base pressures are measured using 16 port - 15 psid electronic pressure scanners. Four

base pressure measurements are made on the core and one on each SRB. Base pressure measurements are then used to remove base pressure effects from the drag and yawing moment terms.

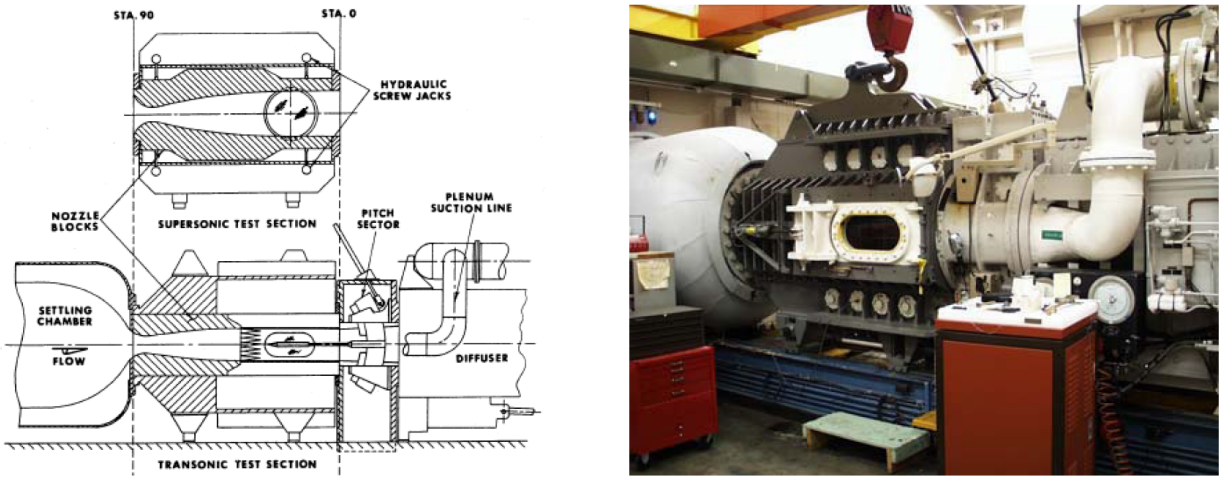

Figure 13. 14" TriSonic Wind Tunnel at MSFC Aerodynamic Research Facility.

B. Vehicle-I Results

All 480 cases were initially simulated using Cart3D since these inviscid computations are relatively inexpensive and the results can be used to identify any obvious problems in setting up the cases. OVERFLOW was used to simulate 144 of the cases within the experimental run matrix, including four pitching angles ($\alpha_T = -4$, 0, 6, and 10 degrees), three roll angles ($\phi_T = 0$, 45, and 90 degrees), and all twelve Mach numbers. USM3D was run on a subset of 73 cases out of the total 144. All force and moment coefficients were compared in the missile axis coordinate system. Figure 2 shows a diagram containing both the missile axis and body axis coordinate systems.

Focusing on one particular (α_T, ϕ_T) combination, the CFD codes predicted axial, normal and side force over the entire Mach range are plotted on the left column of Figure 14, along with experimental results. The right column of Figure 14 plots the percent difference between CFD and experiment. Additionally, a shaded area representing measurement uncertainty is included in the percent difference plots for axial and normal force (no uncertainty measure was provided for side force). Both OVERFLOW and USM3D predict larger axial force, but are within approximately 12% of the experiment, discounting the differences at Mach 1.46 due to abnormality in the experimental data. USM3D consistently predicts larger axial force coefficients than OVERFLOW. Cart3D results have qualitatively similar behavior to the experimental results, but predict lower axial forces for Mach numbers above 2.0, due to the lack of viscous contributions. However, this behavior is not observed in the transonic regime where Cart3D predicts larger axial force coefficients compared to the other data. Viscous results for normal force are within 10% of the experiment and are almost inside the measurement uncertainty margin over the entire Mach range. The inviscid result is again qualitatively reasonable, but off by about 10% to 20% over the entire Mach range. All of the CFD solvers predict lower side forces in the supersonic regime, while the viscous solvers predict higher and Cart3D predicts lower side forces in the subsonic and transonic regimes. In fact, all of the CFD codes differ by about 10% to 20% compared to the experiment. Even though the side force validation is somewhat poor, OVERFLOW and USM3D match each other particularly well for each of the force coefficients. Similar trends are observed over the entire (α_T, ϕ_T) parameter space. For example, the axial force is compared in Figure 18 (a) for $\alpha_T = 0^\circ$ and $\phi_T = 0^\circ$. The results are almost identical to the results shown in 14 (a), where only a slight difference is observed for the Cart3D result at Mach 0.9.

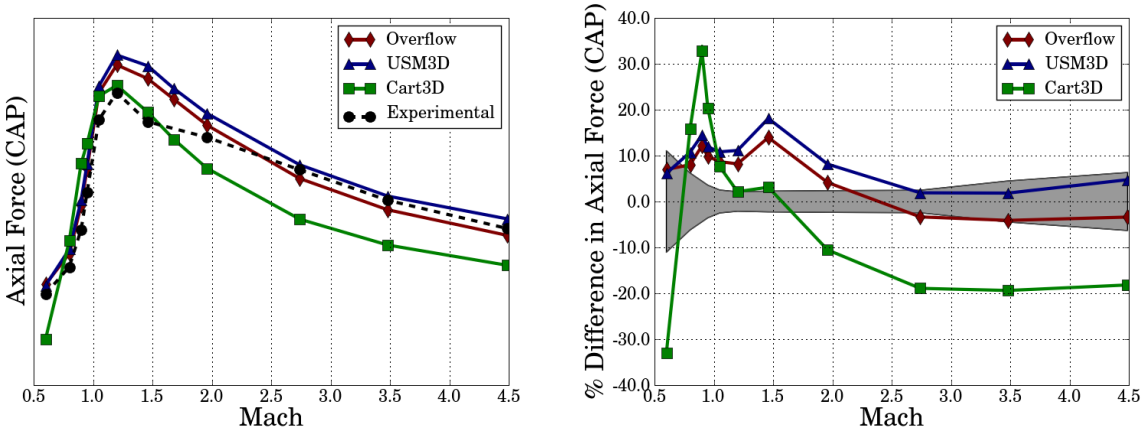

(a) Axial Force

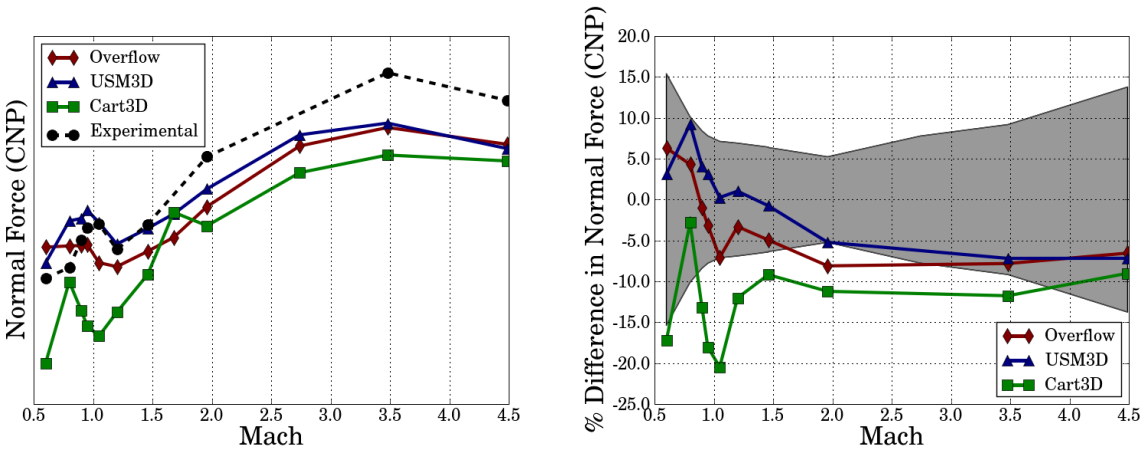

(b) Normal Force

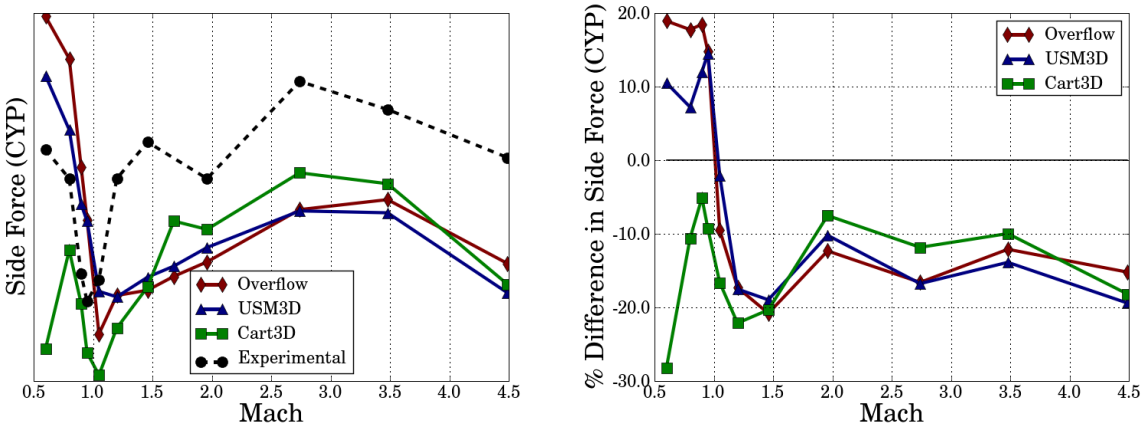

(c) Side Force

Figure 14. Comparison of CFD codes and experimental data for Vehicle-I, showing unscaled forces (left), and percent difference in forces from experimental (right), versus Mach number at $\alpha_T = 6°$, $\phi_T = 45°$ orientation. The shaded region in the right-side plots represents the uncertainty in experimental balance measurements.

C. Vehicle-II Results

For the Vehicle-II wind tunnel test article, the bi-conic shroud section of the vehicle was replaced with a tangent ogive shape. A comparison of the two spherically-blunted shapes is shown in Figure 15. The design change was made after a shape trade study conducted with the Saturn V rocket identified significant drag reduction benefits with the tangent-ogive shape.[27] Figure 18 (b) plots the axial force coefficient in the body axis at $\alpha = 0°$ and $\beta = 0°$ for OVERFLOW, USM3D, and the experiment on the left, and the percent difference to the experiment on the right. The left figure shows that USM3D predicts larger axial force coefficients than OVERFLOW, but unlike Vehicle-I the axial force is not always larger than the experimental result. OVERFLOW's percent difference is within 10% across the entire Mach range except near Mach 0.6, but this is where the largest measurement uncertainty exists. The USM3D result at Mach 0.6 is also different by 15% to 20% across the entire subsonic regime. More interesting is the difference between the OVERFLOW and USM3D results in the subsonic regime. This results in a large amount of uncertainty in both the CFD and experimental results for the low subsonic regime for this vehicle design and further study is necessary to explore the reason behind these differences. Good comparisons between both viscous CFD codes and the experiment are obtained over the rest of the Mach number range.

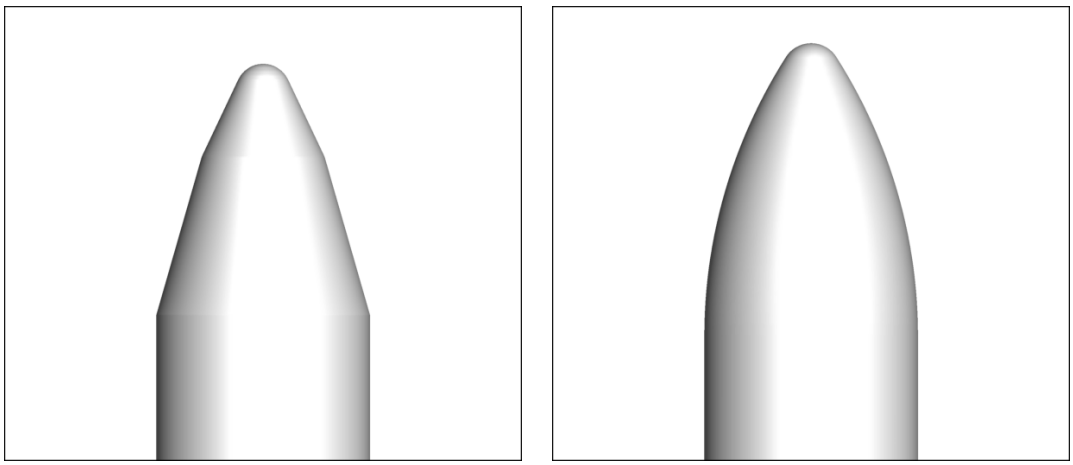

Vehicle-I Shroud | Vehicle-II & Vehicle-III Shroud

Figure 15. Shroud section of the geometry showing the difference between the bi-conic shape used in Vehicle-I (left) and the tangent ogive shape used in Vehicle-II (right)

D. Vehicle-III Results

The Vehicle-III wind tunnel test article retained the tangent ogive shape of the Vehicle-II shroud section, but adds fairings to the aft section of the core. The additional fairing adds a small amount of frontal area to the vehicle and significantly changes the shape of the base region, as shown in Figure 16. Figure 18 (c) plots the body axis axial force coefficient at $\alpha = 0°$ and $\beta = 0°$ for OVERFLOW, USM3D, and the experiment on the left and the percent difference from the experiment on the right. Again, the largest measurement uncertainties occur in the low speed region of the trajectory. In the left figure, the axial force comparisons are very consistent with the Vehicle-II study. For example, OVERFLOW and USM3D have the same qualitative behavior. OVERFLOW predicts lower forces than the experimental result in the low subsonic and high supersonic regimes, while predicting higher forces in the transonic regime. USM3D predicts higher through the subsonic, transonic, and low supersonic, then predicts lower in the high supersonic regime. The percent differences in the left plot of Figure 18 (c) show similar behavior as Vehicle-II. Again, the supersonic cases compare better than the low subsonic cases, but compared to Vehicle-II, percent differences are a factor of two larger between the experiment and CFD results. This difference is likely due to the procedure in which the base pressure is removed from the axial force coefficient in the experimental results. The experimental forces for the fore-body section of the vehicle are computed by subtracting an averaged base pressure force

from the total axial force. Six pressure taps are used to compute the averaged pressure on the base. The locations of the pressure taps are shown in the bottom of Figure 16. It is observed from the CFD solutions of Figure 17 that the base pressure is less uniform with the addition of the fairings. This implies that the experimental averaging procedure is less accurate for Vehicle-III, and more pressure taps may be necessary to accurately approximate the averaged base pressure. In subsonic flow, small base pressure errors cause large percent differences the force coefficients, since the magnitudes of the coefficient is small in this regime. Note the uncertainty associated with this procedure is not included in the measurement uncertainty.

VII. Summary

A computational approach for generating aero-databases of heavy lift launch vehicle ascent has been described. Sensitivity and validation procedures are outlined and have been applied to three independent CFD codes: OVERFLOW, USM3D, and Cart3D. The best practice procedure includes sensitivity analyses for each code. The first step is to establish a grid-independent solution before studying the effects of turbulence models and/or flux-differencing schemes. Once consistent parameters are individually established for each CFD solver, a code-to-code comparison should be performed. After acceptable code-to-code comparisons are achieved, the CFD results should be validated with experimental or flight data.

In this study, the best practice protocol was applied to Ares V aerodynamic ascent database generation. Initial studies established grid resolution requirements for each code. Force and moment coefficients predicted with the SA and SST turbulence models showed insignificant sensitivity to turbulence model. Small variations were observed between central and upwind differencing schemes, but these variations were less than the established engineering tolerance. These results defined the CFD best practices for HLLV ascent simulations, and were applied to aero-database generation for three design cycles of the Ares V.

Experimental test data was used to validate the Vehicle-I aero-database generation procedure for all three codes. Strong agreement was observed between the two viscous codes which were within 15% of the experimental data, while the inviscid code consistently predicted force and moment coefficients within 30% of the viscous results. Subsequently, databases were generated for full-scale HLLVs, Vehicle-II and Vehicle-III. Scaled-down versions of these two vehicles were tested in the TriSonic Wind Tunnel to provide additional validation data. Geometry differences in the vehicles' aft-regions created base pressure variations which led to greater uncertainty in the subsonic comparisons. Lessons learned from this sensitivity and validation study will be used to generate future rocket ascent aero-databases. This study should be extended further to properly model plume and protuberance effects.

VIII. Acknowledgments

The authors acknowledge the support of the Ares V Project at MSFC for providing CAD geometry and trajectory data, as well as funding for the project. The authors also thank the Ares Aero Panel members for valuable discussions regarding the results of the present work, and Dr. William Chan for providing guidance and help with the overset grid tools. Computations were performed on NASA Advanced Supercomputing (NAS) platforms at Ames Research Center.

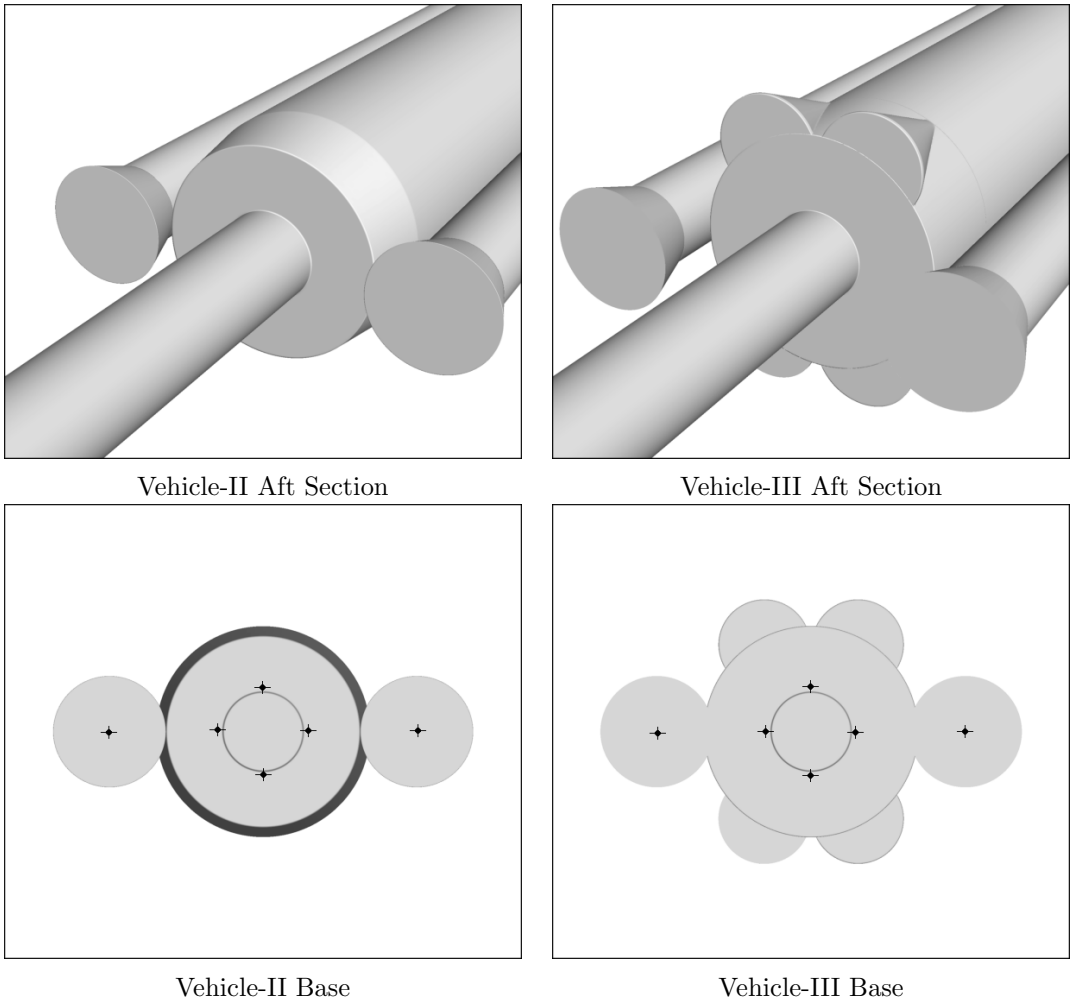

Figure 16. Aft and base sections of the geometry showing the difference between Vehicle-II (left) and Vehicle-III (right). Point locations for the pressure taps used in the experimental measurements are also included.

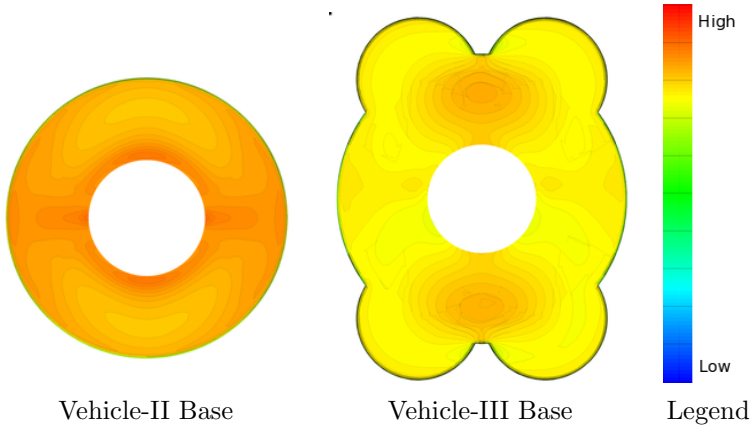

Figure 17. Pressure on the base of the core section showing differences between Vehicle-II (left) and Vehicle-III (right) at $\alpha = 0°$ and $\beta = 0°$.

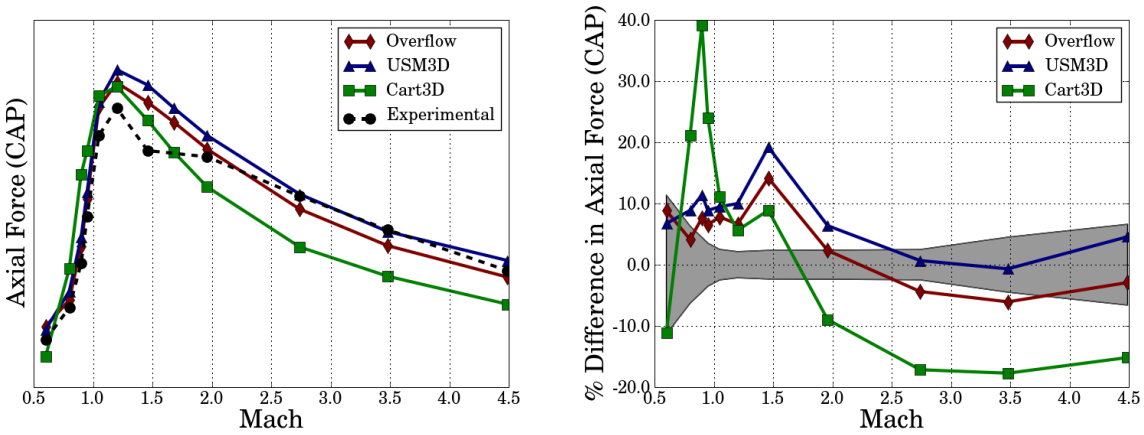

(a) Vehicle-I

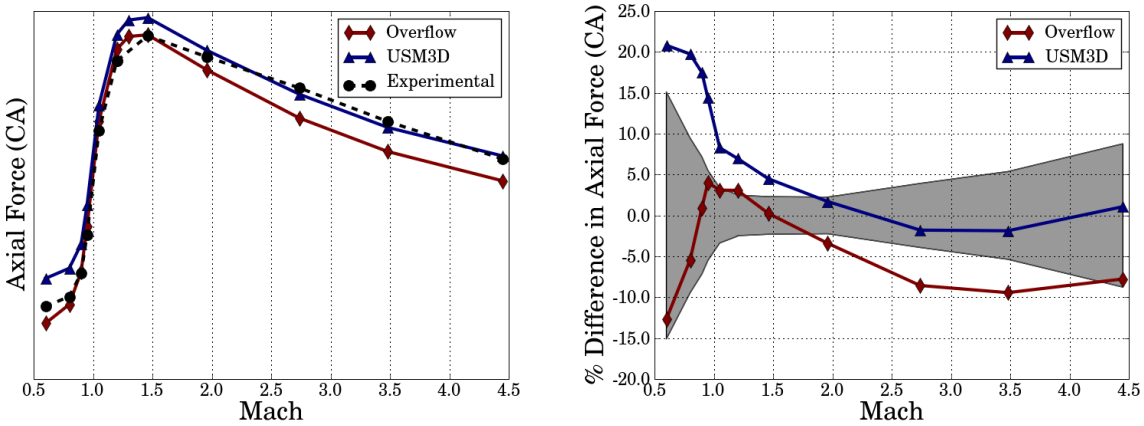

(b) Vehicle-II

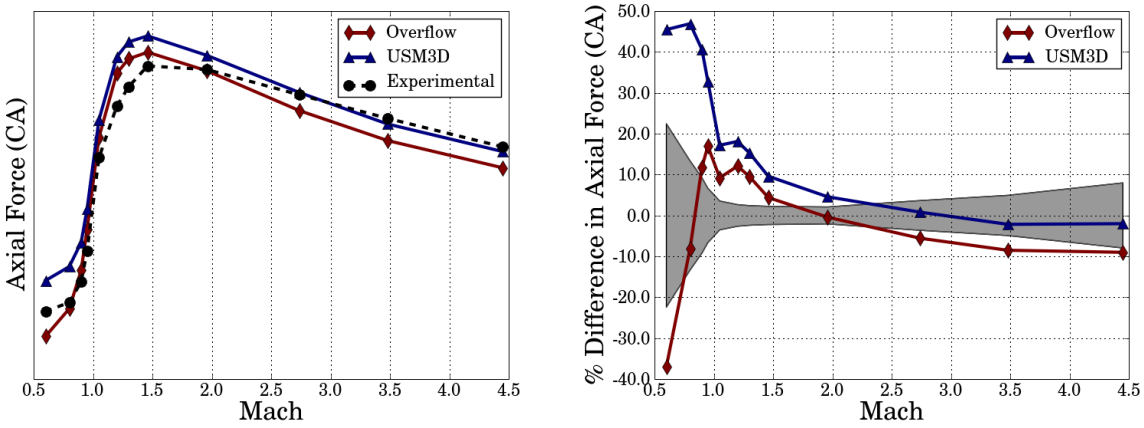

(c) Vehicle-III

Figure 18. Comparison of CFD codes and experimental data for three wind tunnel models, showing unscaled forces (left), and percent difference in forces from experimental (right), versus Mach number at zero angle of attack ($\alpha_T = 0°$, $\phi_T = 0°$, and $\alpha = 0°$, $\beta = 0°$). The shaded region in the right-side plots represents the uncertainty in experimental balance measurements.

References

[1]NATO Advisory Group for Aeronautical Research and Development, "Validation of Computational Fluid Dynamics," December 1988, AGARD CP 437.

[2]American Institute of Aeronautics and Astronautics, "AIAA Guide for the Verification and Validation of Computational Fluid Dynamics Simulations," 1998, G-077-1998e.

[3]Roache, P., *Verification and Validation in Computational Science and Engineering*, Hermosa Publishers, 1998.

[4]Spalart, S. and Allmaras, S., "A One-Equation Turbulence Model for Aerodynamic Flows," *30th Aerospace Sciences Meeting and Exhibit, Reno, NV*, January 1992, AIAA 92-0439.

[5]Menter, F., "Zonal Two Equation k-ω Turbulence Models For Aerodynamic Flows," *23rd Fluid Dynamics, Plasmadynamics, and Lasers Conference, Orlando, FL*, July 1993, AIAA 93-2906.

[6]Jameson, A., Schmidt, W., and Turkel, E., "Numerical solution of the Euler equations by finite volume methods using Runge Kutta time stepping schemes," *14th Fluid and Plasma Dynamics Conference, Palo Alto, CA*, June 1981, AIAA 81-1259.

[7]Pulliam, T., "Artificial dissipation models for the Euler equations," *AIAA Journal*, Vol. 24, No. 12, 1986.

[8]Roe, P., "Approximate Riemann Solvers, Parameter Vectors, and Difference Schemes," *J. Computational Physics*, Vol. 43, 1981, pp. 357–372.

[9]Van Leer, B., "Towards the Ultimate Conservative Difference Scheme V. A Second Order Sequel to Godunov's method," *J. Computational Physics*, Vol. 32, 1979, pp. 101–136.

[10]Liou, M., "A New Flux Splitting Scheme," *J. Computational Physics*, Vol. 107, 1993, pp. 23–39.

[11]Nichols, R., Tramel, R., and Buning, P., "Solver and Turbulence Model Upgrades to OVERFLOW 2 for Unsteady and High-Speed Applications," *24th AIAA Applied Aerodynamics Conference, San Francisco, California*, June 2006, AIAA 2006-2824.

[12]Nichols, R. and Buning, P., "User's Manual for OVERFLOW 2.1," Version 2.1t.

[13]Frink, N., "Upwind Scheme for Solving the Euler Equations on Unstructured Tetrahedral Meshes," *AIAA Journal*, Vol. 30, No. 1, 1992, pp. 70–77.

[14]Frink, N., "Tetrahedral Unstructured Navier-Stokes Method for Turbulent Flow," *AIAA Journal*, Vol. 36, No. 11, 1998, pp. 1975–1982.

[15]Aftosmis, M., Berger, M., and Adomavicius, G., "A Parallel Multilevel Method for Adaptively Refined Cartesian Grids with Embedded Boundaries," *38th Aerospace Sciences Meeting and Exhibit, Reno, NV*, Jan 2000, AIAA 2000-0808.

[16]Nemec, M. and Aftosmis, M., "Adjoint Error Estimation and Adaptive Refinement for Embedded-Boundary Cartesian Meshes," *18th AIAA Computational Fluid Dynamics Conference, Miami, Florida*, June 2007, AIAA 2007-4187.

[17]Gomez, R. and Ma, E., "Validation of a Large Scale Chimera Grid System for the Space Shuttle Launch Vehicle," *12th AIAA Applied Aerodynamics Conference, Colorado Springs, CO*, June 20-22 1994, AIAA-1994-1859.

[18]Chan, W., Gomez, R., Rogers, S., and Buning, P., "Best Practices in Overset Grid Generation," *32nd AIAA Fluid Dynamics Conference and Exhibit, St. Louis, Missouri*, Jun 24-26 2002, AIAA-2002-3191.

[19]McMillin, S. and Frink, N., "Assessment of Data Issues from LAV 19-AA Wind Tunnel Test Using TetrUSS," Task CAP-AR-41, EG-CAP-07-85, July 2007.

[20]Pao, S., Vatsa, V., Abdol-Hamid, K., Pirzadeh, S., J.A., S., Klopfer, G., and Taft, J.R. an Parlette, E., "Best Practice for Ascent Aero Analysis for the Ares I Configurations," *JANNAF-55*, 2008.

[21]Aftosmis, M. and Nemec, M., "Simulation Guidelines: LAV Meshing and Convergence Studies with Cart3D," Nov. 2007, https://ice.exploration.nasa.gov/Windchill/netmarkets/jsp/object/view.jsp?oid=bookmark%7Ewt.workflow.notebook.ImportedBookmark%3A409925566&u8=1[1].

[22]Pandya, S., Chan, W., and Kless, J., "Automation of Structured Overset Mesh Generation for Rocket Geometries," *19th AIAA Computational Fluid Dynamics Conference, San Antonio, Texas*, Jun 22-25 2009, AIAA-2009-3993.

[23]Gusman, M., Housman, J., and Kiris, C., "Best Practices for CFD Simulations of Launch Vehicle Ascent with Plumes," *49th AIAA Aerospace Sciences Meeting, Orlando, Florida*, Jan 4-7 2011, Accepted.

[24]Deere, K., Elmiligui, A., and Abdol-Hamid, K., "Best Practices for CFD Simulations of Launch Vehicle Ascent with Plumes - USM3D Perspective," *49th AIAA Aerospace Sciences Meeting, Orlando, Florida*, Jan 4-7 2011, Accepted.

[25]Simon, E., "The Georce C. Marshall Space Flight Center's 14 × 14-Inch Trisonic Wind Tunnel Technical Handbook," NASA Technical Memorandum TM X-64624, NASA/MSFC, 1971.

[26]Spring, A. M., "Uncertainty Analysis of the NASA MSFC 14-Inch Trisonic Wind Tunnel," *37th AIAA Aerospace Science Meeting and Exhibit, Reno, NV*, Jan 11-14 1999, AIAA-1999-0684.

[27]Gusman, M., Housman, J., and Kiris, C., "Adjoint-Based Adaptive Meshing in a Shape Trade Study for Rocket Ascent," *6th International Conference on Computational Fluid Dynamics, St. Petersburg, Russia*, July 12-16 2010.